Electron capture and loss in the scattering of low-energy protons with a C_{60} monolayer deposited on Cu(111)

V. Quintero Riascos,[1] M. Tacca,[1] R. Vidal,[1,2] C. Gonzalez,[3,4] E. C. Goldberg,[1] and F. Bonetto[1,2,*]
[1]*Instituto de Física del Litoral (CONICET-UNL), Güemes 3450, S3000GLN Santa Fe, Argentina*
[2]*Departamento de Física, Facultad de Ingeniería Química, Universidad Nacional del Litoral, Santiago del Estero 2829, S3000AOM Santa Fe, Argentina*
[3]*Departamento de Física de Materiales, Universidad Complutense de Madrid, E-28040 Madrid, Spain*
[4]*Instituto de Magnetismo Aplicado UCM-ADIF, Vía de Servicio A-6, 900, E-28232 Las Rozas de Madrid, Spain*

(Received 30 July 2020; revised 18 March 2021; accepted 12 May 2021; published 8 June 2021)

Final projectile charge states are experimentally and theoretically analyzed after H^+ ions collide with a C_{60} monolayer deposited on Cu(111) with an ample range of incoming energies (2–8 keV) in the low-energy regime. The three possible charge states (negative, positive, and neutral) are experimentally measured by using the low-energy ion scattering technique for two different collisional setups: 45° (90°) and 67.5° (67.5°) incoming (exit) angles, relative to the target surface plane, with a fixed backscattering angle of 135°. Experimental ion fraction magnitudes and energy dependence are practically intermediate between that found in pristine Cu(111) and a thick C_{60} film, revealing the influence of the substrate on the final charge state of the projectile. Unlike these previous systems, the positive and negative ions contribute nearly evenly to the total scattered charged particles. On the theoretical side, we applied a first-principles based model that considers the fine details of the surface under analysis and assumes a projectile trajectory corresponding to a single binary collision with the more exposed carbon atoms of the C_{60} molecule. The theoretical and experimental results are independently compared with the already reported cases: H^+ on a thick C_{60} film, H^+ on Cu(111), and H^+ on graphite. A detailed analysis of the electronic surface band structure allows us to draw a conclusion about the relevance of the substrate in the present system and about the aspects to be improved in our theoretical description. The contrast between experimental and theoretical results allows us to infer that trajectories involving ion penetration and multiple scattering events are particularly relevant for the projectile-target charge exchange process studied.

DOI: 10.1103/PhysRevA.103.062805

I. INTRODUCTION

Charge exchange between atoms and surfaces in dynamic situations involves physical and chemical processes extensively explored in the literature [1–5]. However, some questions remain unclear, deserving active current research [6–13]. For example, the quantitative relevance of each individual physical parameter involved in the charge transfer process in a particular projectile-target system cannot be precisely envisaged. Recently, it has been shown that charge exchange affects the scattering potential of the ion-target system, influencing then the inelastic and elastic energy transfer in low-energy collisions. This effect is especially important in the very first monolayer of the surface, becoming then particularly relevant for two-dimensional (2D) materials [14]. These variations in the elastic and inelastic energy transfer become experimentally evident when the electronic energy loss of He ions and protons transmitted through single-crystalline silicon foils is compared for channeled and random trajectories [15].

Even when determining the final charge state of a projectile after being scattered by a target surface presents an inherent fundamental motivation, the problem also presents relevance in applied research fields. For instance, it is a key issue in particle detectors design [16], film deposition for devising new materials [17], plasma-wall interactions in nuclear fusion reactors [18,19], and heterogeneous catalysis in the chemical industry [20,21]. Recently [8], it was shown that charge exchange processes in low-energy ion-surface collisions are a key issue in achieving direct deoxygenation of carbon dioxide after being scattered by surfaces.

Due to their wide extent of applications, fullerenes have been widely studied [22]. Although the uses of fullerenes cover broad areas of science and technology, their applications in biomedicine are definitively noteworthy: They include the design of contrast agents for magnetic resonance and x-ray imaging, drug and gene delivery, and photodynamic therapy [23]. Other fields where usage of fullerenes has been proposed are medicine for tumor cell treatment [24], electronics [25], dermatology [26], and in energy generation due to its applications in organic solar cell based devices [27]. In addition, the proved presence of C_{60} and $C_{60}{}^+$ in interstellar space [28], where collisions with energetic hydrogen ions is likely, makes the charge exchange in proton-C_{60} dynamic interaction of relevance in astrophysics.

Experimentally, the final charge state of a given projectile colliding with a particular surface depends on two independently controlled factors: the incoming energy of the projectile

---

[*] Corresponding author: bonetto@santafe-conicet.gov.ar

and the geometrical setup (incoming and exit angles) of the collisional system. From them, it is possible to obtain a couple of key parameters in the charge transfer problem: the projectile velocity components perpendicular and parallel to the surface plane. While the relevance of the perpendicular component is primarily associated with the projectile-surface interaction time and the distance of closest approach, the parallel component allows for sensing the different features of the electronic surface band structure and the surface topology of the target [29–33].

The electronic properties of a fullerene film strongly depend on its thickness and the physical properties of the substrate where it is deposited [34,35]. The Cu(111) substrate presents an electronic structure with two main distinctive features: a surface state located within the L-gap, and a marked dispersion in the parallel component of the wave number, $k_{//}$ [36]. It has been observed that the electronic band structure of a C_{60} monolayer (ML) is strongly influenced by the Cu(111) substrate, when compared to that of a thick C_{60} film [37–39]. The onset of an interfacial state close to the Fermi level confers metallic properties to the C_{60} monolayer film, rather different from that of a thick C_{60} film. All these features could lead to electronic exchange processes that depend on the specific location of the scatter carbon atom on the C_{60} molecule adsorbed in the substrate. Site dependence of charge exchange has been experimentally observed in the collision of He^+ projectiles with noble metals [40,41].

In a previous paper [42], we showed the major relevance of the peculiar features of the Cu(111) surface electronic band structure in the final charge state of protons colliding with this surface. On the other side, in a recently published study [6] we showed that the Cu(111) substrate does not play any significant role in the dynamic charge exchange problem when a three-layer C_{60} film is deposited on it. In the present study we aim to investigate if and how the modified electronic properties of the C_{60} monolayer alter the final charge state of protons scattered by this surface. For this purpose, low-energy ion scattering (LEIS), one of the most surface-sensitive techniques, is used to determine the final charge state of H^+ projectiles after being scattered by a C_{60} monolayer grown on Cu(111). Low incoming energies and low irradiation doses are essential to avoid fragmentation of the C_{60} molecules during the experiment [43]. Positive, negative, and neutral hydrogen ion fractions are measured for a wide energy range (2–8 keV) and for two incoming (exit) angles: 45° (90°) and 67.5° (67.5°) (with a fixed scattering angle of 135°). The selection of these incoming (exit) angles allows us to experimentally explore the relevance of different trajectories on the charge exchange during the ion-surface collision.

A theoretical approach based on the Anderson model [44] was used to describe the resonant charge exchange occurring in the single binary collision between protons and carbon atoms that belong to a C_{60} monolayer deposited on Cu(111). This model accounts for the details of the surface [C_{60} monolayer plus Cu(111) substrate] band structure and the three possible projectile charge states in a time-dependent quantum process, where the electronic repulsion in the localized projectile state is considered up to second order in perturbation theory [45]. This model with its approximations has succeeded in describing the charge exchange process of H^+ projectiles interacting with other carbonaceous targets [6,46,47].

As in H-Cu(111) and H-thick C_{60} film systems, the total experimental ion fraction ranges from 10% to 20% (neutralization between 90% and 80%) for the whole energy range and for both geometrical configurations. Unlike the previously studied systems, a predominance of the positive or negative ion fractions (ranging between 5% and 10%) for the whole energy range is not observed in any of the geometrical configurations studied.

Since a major contribution of H^+ projectiles directly colliding with the substrate is expected in the measured ion fractions, theoretical and experimental results are indirectly and qualitatively compared to get an insight into the relevance of these collisions in the final projectile charge state. Alternatively, an independent comparison of the theoretical results with previously studied projectile/target systems [H-Cu(111) and H-thick C_{60} film] allows us to draw a conclusion about the relevance of the electronic band structure of the different surfaces. We also discuss possible improvements in the theoretical model applied and/or the proper experimental setup to match the assumptions made in the calculations.

II. EXPERIMENT

A. Sample preparation and characterization

C_{60} powder placed on a Knudsen cell was deposited on a previously cleaned and annealed Cu(111) monocrystal substrate via sublimation under ultrahigh-vacuum (UHV) conditions ($\sim 10^{-10}$ Torr), as described in Ref. [6]. As shown in Ref. [43], by observing the Auger C_{KLL} and Cu_{LVV} signal intensities as a function of the evaporation time, it is possible to determine the time needed to grow the first, second, and upper C_{60} layers on the Cu(111) substrate. As the time needed to obtain a monolayer strongly depends on other experimental parameters, such as the evaporator-substrate distance and the Knudsen cell temperature, we use an alternative procedure to grow a single C_{60} monolayer. On the first stage, a thick C_{60} film (3 ML or more) is evaporated on the substrate. Then, the second and upper layers are thermally desorbed by heating the sample at 650 K. In this way, we can guarantee that only the first monolayer remains attached to the Cu(111) surface, as demonstrated by the Auger desorption curve shown in Fig. 1 (left panel) [43].

In order to characterize the film obtained, we acquired low-energy electron diffraction (LEED) images in the three stages of the film formation (see Fig. 1, right panel) (a) before C_{60} evaporation [pristine Cu(111)], (b) after C_{60} evaporation (thick C_{60} film), and (c) after thermal desorption of the second and upper layers [C_{60} monolayer film on Cu(111)]. The LEED patterns are completely different in these three stages and allow us to verify the quality of the 1 ML C_{60} film formed [43]. A well-known (4 × 4) superstructure pattern is obtained when a unique C_{60} monolayer is deposited on Cu(111) [48]. The C_{60} molecules in the first monolayer are adsorbed in positions that "copy" the symmetry of the fcc(111) copper crystal structure, favored by the fact that the C_{60} molecular van der Waals diameter (10 Å) is about 4 times the Cu-Cu interatomic distance (2.56 Å) in the Cu(111) face [22].

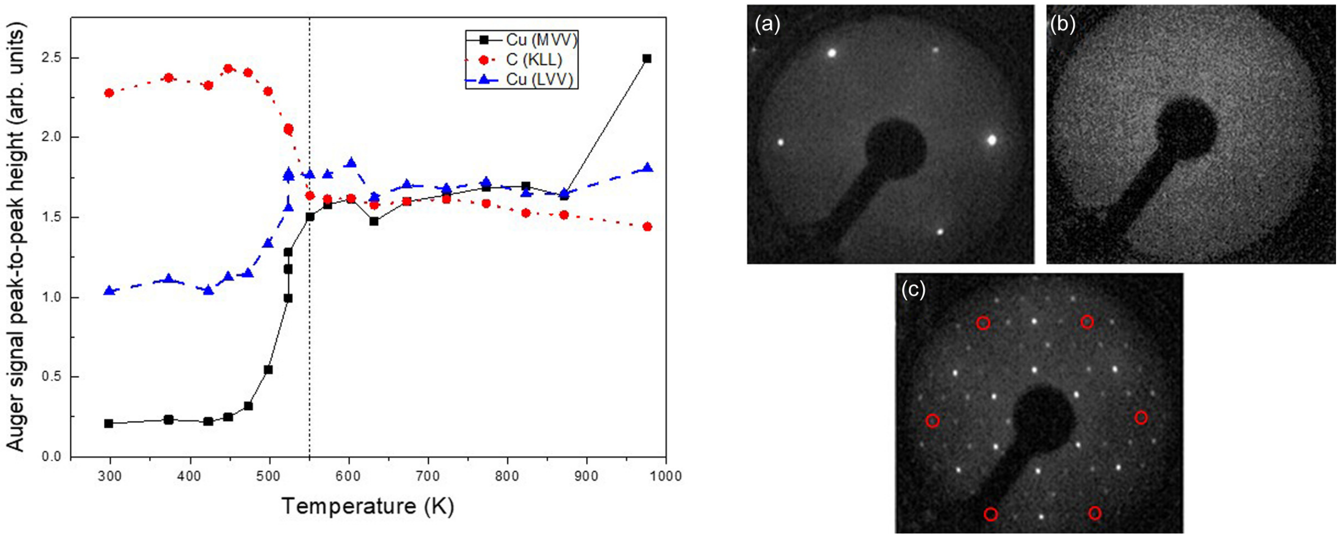

FIG. 1. Left: Cu_{MVV}, Cu_{LVV}, and C_{KLL} Auger peak to peak heights of a thick C_{60} film deposited on Cu(111) as the sample temperature is increased and the upper C_{60} layers are desorbed. At around 550 K, a unique monolayer remains attached to the Cu(111) substrate. Right: LEED patterns obtained for pristine Cu(111) before deposition of a thick C_{60} film (a), after deposition of a thick C_{60} film (b), and after desorption of the upper C_{60} layers (c). The typical (4×4) superstructure for a monolayer C_{60} film deposited on Cu(111) is obtained [48], where the corresponding (1×1) spots are circled (red).

The orientation of the sample was also determined by LEED. The original Cu(111) pristine pattern serves as a reference for the (4×4) C_{60} ML pattern, allowing a precise determination of the azimuthal angle of the sample relative to an axis normal to the target surface [49,50].

Coverage of the substrate by the C_{60} ML film was verified by taking LEED images distributed in an ample region of the sample. Consistency between the obtained patterns was observed all over the sample.

The presence of impurities on the clean Cu(111) was found to be negligible via Auger spectroscopy (AES) and LEIS, and the same negligible impurity amount is expected when the final film is deposited. Minor damage of the C_{60} films due to proton irradiation is estimated for the irradiation dose and projectile incoming energies used in the present study [43].

Sample preparation, characterization, and charge exchange experiments were carried out under the same UHV conditions since all the used techniques (AES, LEED, and LEIS) as well as the Knudsen evaporator are available in the same vacuum chamber.

B. Measurements of ion fractions

A time of flight (TOF) low-energy ion scattering spectrometer [51,52] was used to measure the ion fractions of the scattered hydrogen projectiles. Basically, the spectrometer consists of an ultrahigh vacuum (UHV) chamber (base pressure in the 10^{-10} Torr range), an ion source that allows selecting the desired projectile ion, and a TOF detector. As mentioned above, Auger and LEED techniques are also available in the same vacuum chamber.

Once produced in the discharge ion source, H^+ ions are accelerated to the selected energy and mass analyzed using a Wien filter. Detection by TOF [53] essentially consists in measuring the time elapsed since a given projectile ion collides with the target surface until it reaches the detector. To achieve this, the initially continuous incident beam is transformed into a train of small pulses by using a pair of parallel plates placed in front of a collimating slit and connected to a square wave generator. In this way, short duration pulses (∼100 ns wide) are generated. The smaller the pulse width, the better the temporal resolution of the experiment. However, a very narrow pulse also implies a smaller number of incident and scattered particles, that is, a worse signal to noise ratio for the same acquisition time. In this work, the pulse generation rate was fixed at 3 or 10 kHz, depending on the intensity of the signal, to achieve a time resolution around 100 ns in the TOF spectrum.

Using a pulsed beam in the TOF technique greatly reduces surface damage. In our experiments, the doses and irradiation times necessary to obtain each LEIS spectrum led to fluence values ranging from 10^{13} to 2×10^{14} ions/cm^2, depending on the projectile incoming energy. No damage was detected when the sample was exposed to these proton fluence irradiation values after 8 h of continuous experiments [43].

After colliding with the target sample, the H^+ projectile packets are scattered in all directions, but only those particles scattered in the direction of the flight tube finally reach the detector. It consists of a pair of microchannel plates (MCPs) arranged in a chevron configuration, and a set of three parallel rectangular anodes (left, central, and right anodes) placed behind the MCPs. These electron multipliers intensify the signal produced when a particle reaches the detector, via secondary electron emission. The electrons are then collected by one of the anodes (left, central, or right anode, depending on the impinging ion position on the MCPs), and produce an electron pulse that is amplified by a preamplifier (Ortec VT120). It is important to mention that, although the detection efficiency may depend on whether neutral particles or ions are detected, this difference is negligible when working with

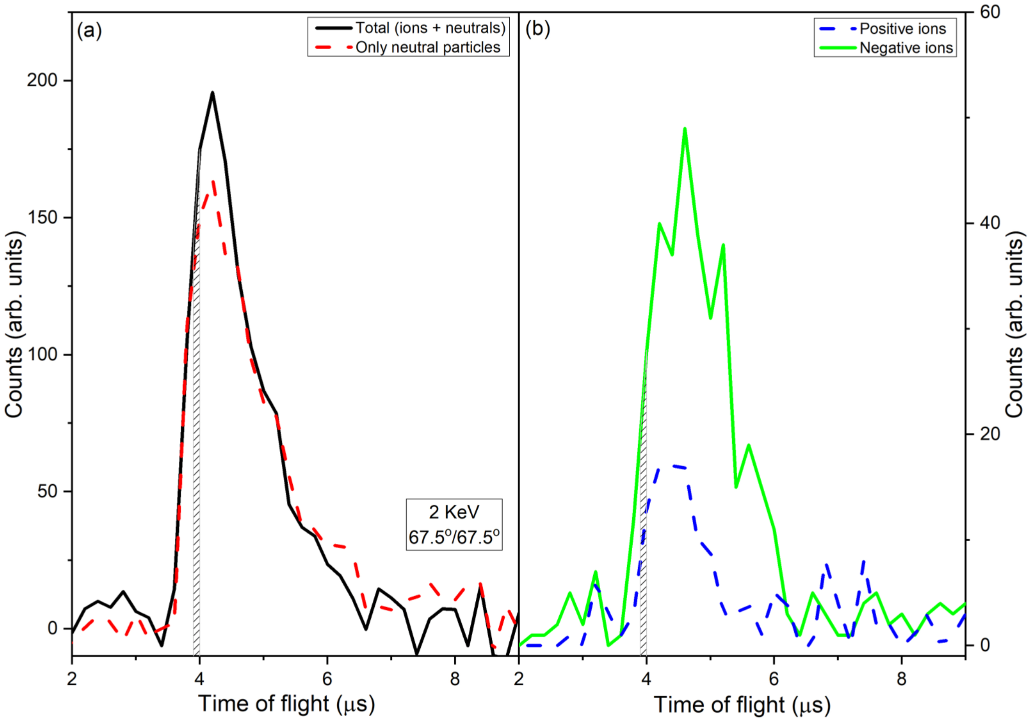

FIG. 2. (a) Background-subtracted TOF LEIS spectra of neutral and total particles scattered when H^+ projectiles collide with a C_{60} monolayer, with an incoming energy of 2 keV and equal incident and exit angles of 67.5°. (b) The corresponding negative and positive ion spectra. The shaded area indicates the elastic peak region considered for the ion fraction calculations. The spectra obtained present contributions from hydrogen projectiles colliding with both carbon atoms of the C_{60} ML and copper atoms from the substrate.

incoming energies higher than 1 keV [54], such as those used in the present work. The positive, negative, and total ion fractions are obtained via two independent experiments: (i) measurement of the total ion fraction and (ii) measurement of positive and negative contributions. In (i), neutral and charged particles are separated by a set of deflection plates located at the entrance of the drift tube and then collected by the central anode mounted at the end of the drift tube. In this way, two spectra are obtained: total (ion plus neutral) and only neutral particles. In (ii), a set of deflection plates located just before the detector allows for discrimination of positive and negative particles, which are finally detected by the same anode (right or left anode). Thus, two spectra are obtained: one for positive and the other for negative ions. The sample-detector distance in our LEIS TOF spectrometer is 157 cm, giving a detector angular acceptance of about 0.4°. The time of flight distributions of the positive, negative, and neutral scattered projectiles are recorded as a histogram (TOF spectrum) by a processor and then, the positive, negative, and total ion fractions are finally determined. The ion fraction values with their corresponding statistical errors are determined from three sets of independent measurements performed for both geometric configurations and each incoming projectile energy.

The C_{60}/Cu(111) sample was fixed on a sample holder that allows for continuous variations of the incident (α), exit (β), and azimuthal (ϕ) angles. The scattering angle subtended by the incoming and exit directions, θ, was kept constant in a backscattering configuration, $\theta = 135°$. Then, the experimental geometrical setup was as close as possible (consistent with our present experimental constraints) to the normal incident and exit geometry assumed in the theoretical model, in which $\theta = 180°$. Two sets of incoming (exit) angles, measured with respect to the target surface plane, were chosen: α (β) = 67.5° (67.5°) and α (β) = 45° (90°) (see Fig. 3). Both configurations present a common feature with the theoretical model: The former [α (β) = 67.5° (67.5°)] fulfills the specular condition assumed in the theory [in which α (β) = 90° (90°)]; in the latter [α (β) = 45° (90°)] the experimental and theoretical exit angles, β, are exactly the same. In this way, by qualitatively comparing experimental with theoretical results, it will be possible to infer which of these features are more relevant for the charge transfer process description. A single azimuthal direction, $\phi = 30°$ (consistent with that of Refs. [42,55]), was set for the ion fractions measurements. Based on previous results [6], a negligible dependence on the azimuthal direction is expected.

In Fig. 2 we show the corresponding spectra for total and neutral particles [panel (a)] and positive and negative [panel (b)] contributions for an incoming energy of 2 keV and a 67.5° (67.5°) entrance (exit) angle geometric configuration. Given that the theoretical approach used to describe the experimental results assumes a binary collision between the projectile and the scatter target atom, the experimental ion fractions are determined by considering only a TOF interval in the vicinity of the elastic peak (shaded region in Fig. 2). In this way, we focus only on charge exchange processes that lead to projectile exit energies close to that corresponding to the elastic peak

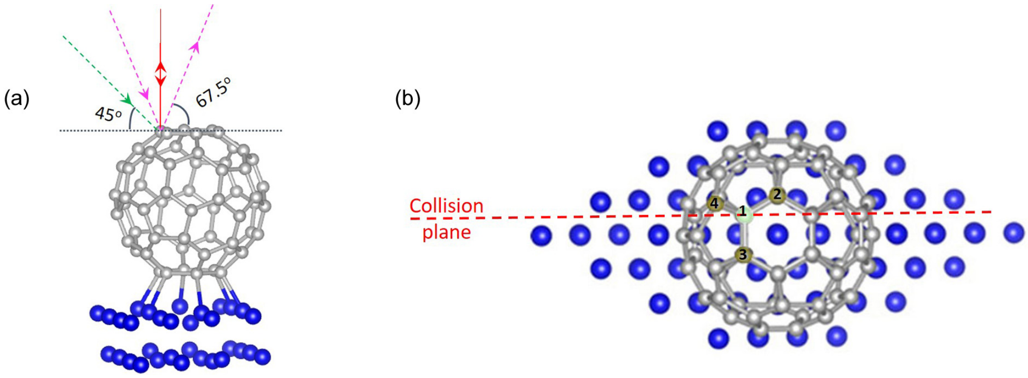

FIG. 3. (a) Lateral view of the C_{60} molecule adsorbed on the Cu(111) substrate. The upper plane is indicated (dotted horizontal line), as well as the two experimental (dashed lines) and the theoretical (solid line) collisional geometries. (b) Upper view of the target sample, where the collision plane (horizontal dashed line) is indicated. The exposed C_{60} hexagon assumed in our calculations can be appreciatted in this view. The scatter atom used in the calculations (atom 1) and its three nearest neighbors (atoms 2, 3, and 4) are shown.

collision with C surface atoms. However, and given that the range of H projectiles at the studied energies is larger than 30 nm (as calculated via SRIM (Stopping and Range of Ions in Matter) code [56]), this selection does not preclude the inclusion of H projectiles interacting with copper atoms and leaving the target with an energy close to that of the H-C elastic peak. Even more, SRIM-based simulations show a relative major contribution of H projectiles colliding with Cu atoms when compared to contributions of single H-C collisions, even at the vicinity of the H-C elastic peak. A larger scattering cross section of copper atoms relative to that of carbon atoms and the highly penetrating H projectiles are the underlying causes of this result [57]. To the best of our knowledge, experimental identification and posterior separation of both contribution is not feasible.

III. THEORETICAL APPROACH

Due to the position of the projectile ionization and affinity levels, within the surface conduction and valence bands, respectively, the charge exchange process during the collision is driven by the resonant mechanism. Details of the calculation model employed are reported in a previous paper [6]; in the following we briefly introduce it. The Anderson-Newns Hamiltonian,

$$\hat{H} = \sum_{\vec{k},\sigma} \varepsilon_{\vec{k}} \hat{n}_{\vec{k},\sigma} + \sum_{\sigma} [\varepsilon_I + U\hat{n}_{a-\sigma}]\hat{n}_{a\sigma} + \sum_{\vec{k},\sigma} [V_{\vec{k}a}\hat{c}^{+}_{\vec{k},\sigma}\hat{c}_{a,\sigma} + \text{H.c.}], \tag{1}$$

is the starting point of our theoretical approach. In Eq. (1), the first term contains information related to the solid target surface, $\vec{k}$ labels the solid band states $\psi_{\vec{k}}$ with energy $\varepsilon_{\vec{k}}$ and occupation number operator $\hat{n}_{\vec{k},\sigma}$, σ being the spin projection. The second term describes the hydrogen projectile, a represents its relevant s-valence orbital, with ionization energy ε_I and electronic repulsion U, while $\hat{n}_{a\sigma}$ is the occupation number operator. The third term represents the interaction between the solid band and the projectile states, where the creation (annihilation) operator $\hat{c}^{+}_{\vec{k}\,\sigma}$ ($\hat{c}_{a\sigma}$) creates (destroys) an electron with spin projection σ in the $\vec{k}$ (a) state. The $V_{\vec{k}a}$ terms account for the interaction between the solid target surface and the projectile atom, and are crucial to our calculation.

When the solid states $\psi_{\vec{k}}$ are expanded in an atomic basis of φ_α orbitals centered on the m atoms of the solid, $\psi_{\vec{k}}(\vec{r}) = \sum_{\alpha,m} c^{\vec{k}*}_{\alpha m}\varphi_\alpha(\vec{r} - \vec{R}_m)$, the $V_{\vec{k}a}$ can be obtained from [44]

$$V_{\vec{k}a} = \langle \psi_{\vec{k}} | V | \phi_a \rangle = \sum_{\alpha,m} c^{\vec{k}*}_{\alpha m} V_{\alpha m,a}(\vec{R}), \tag{2}$$

where the coupling terms between the projectile atom located at the position $\vec{R}$ and a particular target atom positioned at $\vec{R}_m$, $V_{\alpha m,a}(\vec{R}) = \langle \varphi_\alpha(\vec{r} - \vec{R}_m)|V|\phi_a(\vec{r}-\vec{R})\rangle$, are calculated using the bond-pair model [44].

The incoming (exit) trajectories of the projectile ion are assumed to be straight lines, normal to the target surface. As in our previous related studies [6,42], the normal collision assumption is mainly based on a backscattering experimental configuration where the exit angle is normal or close to normal. Measuring the ion fractions for two different geometrical configurations, while keeping fixed the scattering angle, allows us to assess the relevance of this assumption in the present system. The corresponding velocities, $\vec{v}_{\text{in(out)}}$, are taken to be constant and equal to the perpendicular component of the projectile velocity in the corresponding experimental collision geometry. The time $t = 0$ is chosen to be the instant when the projectile reaches the distance of closest approach to the surface, $\vec{R}_{ca}$. Then, the position of the projectile as a function of the time t is given by $\vec{R}_{\text{in(out)}}(t) = \vec{R}_{ca} + \vec{v}_{\text{in(out)}}t$. For a given total projectile energy, the distance of closest approach is determined from the interaction energy between the hydrogen projectile and the carbon atoms [58,59]; i.e., the total energy is considered to calculate this parameter. On the other side, we found a slight dependence of the calculated ion fractions with the distance of closest approach within a reasonable range of projectile-surface distances.

Previous density functional theory (DFT) [60] and scanning tunneling microscope (STM) [61] studies have shown that, due to the hexagonal symmetry of the substrate, the C_{60} buckyballs bond to the Cu(111) substrate via one of their hexagonal faces, leaving the opposite hexagon exposed to the projectile irradiation. In Fig. 3 we sketch the C_{60} molecule attached to the Cu(111) substrate in lateral [Fig. 3(a)] and top [Fig. 3(b)] views. In Fig. 3(a), the ion trajectories of both experimental setups and that of the theoretical approach are shown. In Fig. 3(b), we indicate the selected azimuthal direction in the experimental setup (collision plane) and the scatter C atom chosen in the theoretical model, with its corresponding first nearest neighbors.

The density matrix contains all the information of the target surface required by the theoretical model:

$$\rho_{\alpha m,\beta m'}(\varepsilon) = \sum_{\vec{k}} c^{\vec{k}*}_{\alpha m} c^{\vec{k}}_{\beta m'} \delta(\varepsilon - \varepsilon_{\vec{k}}). \tag{3}$$

The density matrix is calculated through the DFT-based package FIREBALL [62], which uses a linear combination of atomic orbitals (LCAOs) approximation of the solid wave function. Including the time dependence of $\vec{R}$ in $V_{\vec{k}a}$ we obtain

$$V_{\vec{k}a}(t) = \sum_{\alpha,m} c^{\vec{k}*}_{\alpha m} \langle \phi_\alpha(\vec{r} - \vec{R}_m)|\hat{V} e^{i\vec{v}\cdot\vec{r}}|\phi_a[\vec{r} - \vec{R}_a(t)]\rangle e^{-iv^2 t/2}. \tag{4}$$

Then, the $V_{\vec{k}a}$ can be determined by using the coefficients of the density matrix of the surface, $c^{\vec{k}*}_{\alpha m}$, and the atom-atom couplings modulated by the velocity translation factor. In our calculation, and based on geometrical conditions ensuring low parallel components of the projectile velocity, we assume $e^{i\vec{v}\cdot\vec{r}} = 1$ in Eq. (4) [6].

For the ion fractions calculation, we consider that the hydrogen atom can be occupied by up to two electrons. The probabilities of having a negative (P^-), neutral (P^0), or positive (P^+) projectile at time t can be determined by

$$\begin{aligned} P^-(t) &= \langle \hat{n}_{a\uparrow}(t)\hat{n}_{a\downarrow}(t)\rangle, \\ P^0(t) &= \langle \hat{n}_{a\uparrow}(t)\rangle + \langle \hat{n}_{a\downarrow}(t)\rangle - 2\langle \hat{n}_{a\uparrow}(t)\hat{n}_{a\downarrow}(t)\rangle, \\ P^+(t) &= 1 - P^0(t) - P^-(t). \end{aligned} \tag{5}$$

The occupations $\langle \hat{n}_{a\sigma}(t)\rangle$ and $\langle \hat{n}_{a\uparrow}(t)\hat{n}_{a\downarrow}(t)\rangle$ are obtained from the Green-Keldysh functions [63]:

$$\begin{aligned} G_{aa,\sigma}(t,t') &= i\Theta(t'-t)\langle\{\hat{c}^\dagger_{a\sigma}(t'), \hat{c}_{a\sigma}(t)\}\rangle, \\ F_{aa,\sigma}(t,t') &= i\langle[\hat{c}^\dagger_{a\sigma}(t'), \hat{c}_{a\sigma}(t)]\rangle, \end{aligned} \tag{6}$$

where $[\cdots]$ and $\{\cdots\}$ indicate the commutator and anticommutator, respectively; and $\langle\cdots\rangle$ denotes the expectation value over ϕ_o, that describes the system in the Heisenberg representation.

As in our previous studies using hydrogen projectile ions with similar incoming and exit collision angles and the same projectile incoming energy range [6,46], we make the assumption of constant energy levels. This hypothesis is based on an inherent energy width, ΔE_v, associated to the projectile velocity, that is large compared to the atom-surface hybridization width of the projectile a energy level,

$$\Gamma_a(\varepsilon_I) = \pi \sum_{\vec{k}} |V_{\vec{k}a}|^2 \delta(\varepsilon_I - \varepsilon_{\vec{k}}). \tag{7}$$

The ratio between the effective correlation parameter $U^* = U - 2\Delta E_v$ and $\Gamma_a(\varepsilon_I)$ determines the proper approximation for solving Eq. (1) [45]. In the present case, the small-U limit approximation, where the three projectile charge states are calculated via perturbation theory up to second order in the parameter U, was used to calculate the Green's functions (6).

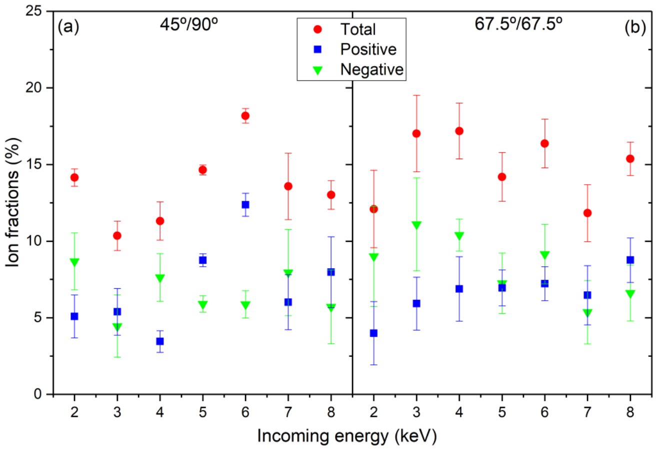

FIG. 4. Total, positive, and negative experimental ion fractions vs incoming H^+ projectile energy for the two explored incoming (exit) angles: 45° (90°) (a) and specular 67.5° (67.5°) (b).

The spatial region where the projectile-surface electronic exchange effectively takes place is determined through the analysis of the characteristic times in a particular collision [6]. In this region, the interaction time $\tau_i \approx \frac{1}{2\Gamma_a}$ (in atomic units), related to the static projectile-surface interaction, should be comparable to the collision time, $\tau_c \approx \frac{1}{v_\perp}$ (in atomic units), associated to the energy width intrinsic to the projectile motion. The evaluation of the characteristic times will also allow us to draw a conclusion about the relevance of the incoming and exit trajectories in the final projectile charge state and to determine the spatial region where the electronic capture and loss processes take place.

IV. RESULTS AND DISCUSSION

A. Experimental results

1. *Measured ion fractions*

Figure 4 shows the measured ion fractions as a function of the projectile incoming energy for the two geometrical configurations employed.

The experimental ion fractions are approximately similar for both analyzed incoming (exit) angles. However, differences in the dependence with the H^+ incoming energy are apparent. While oscillations could be inferred from the erratic dependence obtained for the 45° (90°) configuration, a more defined dependence was obtained for the specular condition, even considering the larger experimental errors obtained. For this configuration, the positive ion fraction slightly increases with projectile incoming energy while the opposite trend is observed for the negative one.

The magnitudes of positive and negative ion fractions are comparable to each other in the whole energy interval analyzed and range from 3% to 12% for both geometrical configurations. However, a slight predominance of negative ions is obtained for the specular geometry at low projectile incoming energies ($\leqslant$4 keV). This trend is not observed for the normal exit configuration, where the scattered negative ion

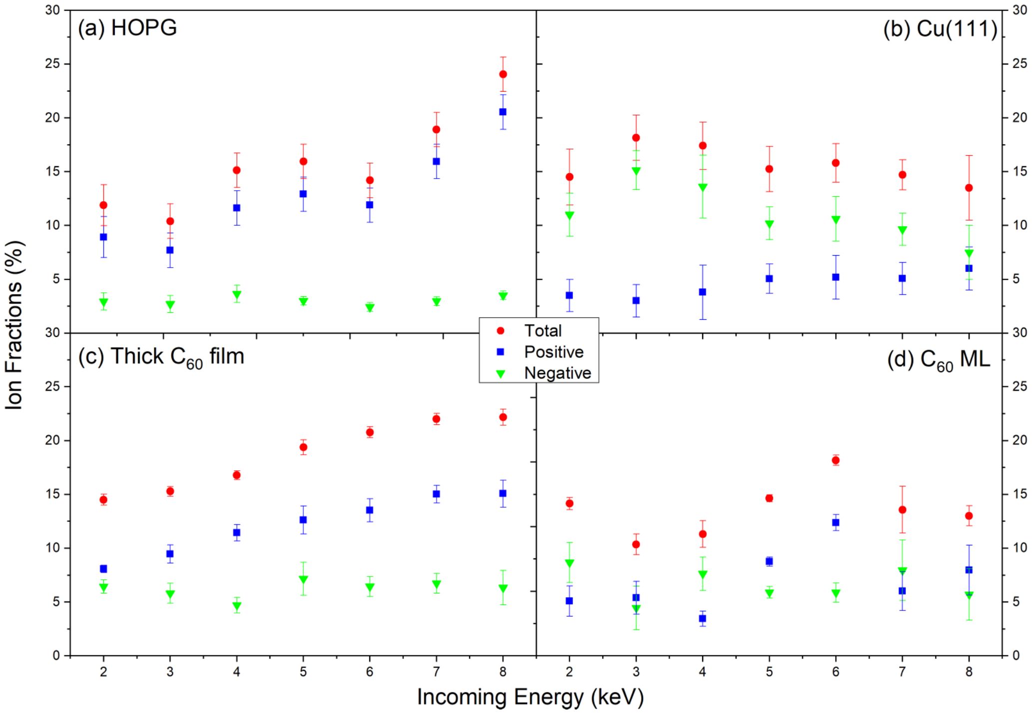

FIG. 5. Comparison of total (red circles), positive (blue squares), and negative (green triangles) experimental ion fractions obtained for four different but related systems: H^+ on HOPG [46] (a), H^+ on Cu(111) [42] (b), H^+ on a thick C_{60} film deposited on Cu(111) [6] (c), and H^+ on a C_{60} monolayer deposited on Cu(111) (d). The measurements correspond to an entrance (exit) angle of 45° (90°).

fraction is nearly constant (around 7%, within the experimental errors) and the positive ion fraction fluctuates between 3% and 12%. Total ion fractions range from 10% to 18% and show an oscillatinglike behavior in both geometrical configurations.

2. Comparison with experimentally studied previous systems

In Fig. 5 we directly compare the final ion fraction obtained when low-energy protons collide with four different surfaces: an highly oriented pyrolytic graphite (HOPG) monocrystalline sample [46], a pristine Cu(111) monocrystal [42], a thick C_{60} film [6], and the C_{60} monolayer system of the present work. All of them were determined following the same experimental procedure and measured under the same experimental conditions: identical scattering and incoming and exit angles.

While a clear predominance of positive scattered ions is observed in protons scattered in an HOPG sample [Fig. 5(a)], a predominance of negative scattered ions is observed when H^+ projectiles collide with a pristine Cu(111) sample in the whole analyzed energy range [Fig. 5(b)]. Ion fractions obtained when protons are scattered by a thick C_{60} film grown on Cu(111) show a similar tendency to that observed in HOPG, that is, an indistinct prevalence of positive scattered ions [Fig. 5(c)]. This result, jointly with the excellent description provided by the theoretical model proposed (that disregards potential collisions with the Cu substrate) [6], strongly indicates that H-C single collisions are of relevance for the charge exchange process, even when detected H projectiles might develop collisions with copper substrate atoms, before passing through the thick C_{60} film. On the other hand, an almost even contribution of positive and negative ions to the final ion fraction is obtained for the C_{60} monolayer film deposited on Cu(111) [Fig. 5(d)]. Contrary to the conclusion drawn for the thick C_{60} film, here the H-Cu collisions are indeed playing an important role in the final charge state of the scattered projectiles. The direct H-C interactions occurring after the projectiles collide with copper substrate atoms and the single binary collisions with C atoms are also determinant, since otherwise the scattered final ion fraction would have presented a prevalence of negative ions, as observed for the clean Cu(111) surface. From this remark, we can expect that our theoretical model, which assumes scattering of the projectile with C atoms only, yields results that overestimate the measured positive ion fractions and underestimate the negative ones.

B. Theoretical analysis

It is important to remark here that with the theoretical model we will calculate the ion fractions that originate when a H^+ projectile binary collides with the most exposed C atoms that belong to the C_{60} monolayer film deposited on a copper substrate. As stated above, these ion fractions should be in principle quite different from the measured ones, which present an important contribution from projectile collisions with copper substrate atoms that, after being backscattered, pass through the C_{60} monolayer film. In this way, the analysis of the calculated ion fractions is only intended to describe how relevant the different elements that enter in our model (surface electronic band structure, surface topology, H-C interaction distance, time, etc.) are for the charge exchange occurring in the collisions of H projectiles with superficial carbon atoms.

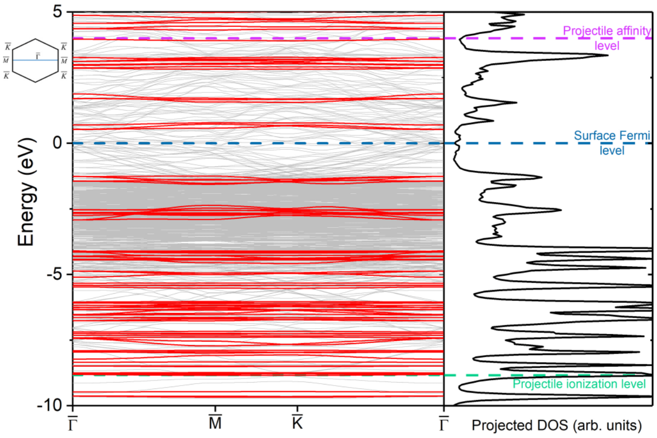

FIG. 6. Left: Band structure of a C_{60} monolayer film deposited on a Cu(111) substrate for the $\overline{\Gamma}-\overline{M}-\overline{K}-\overline{\Gamma}$ path, where the C_{60}-Cu hybridized states (light gray lines) can be appreciated. The band structure of a thick C_{60} film (red thicker lines) is included for comparison. The first Brillouin zone of the 2D reciprocal lattice is shown in the inset. Right: Density of states (DOS) projected on the C_{60} ML film showing the presence of states close to the surface Fermi level. The projectile affinity and ionization levels are also indicated.

The theoretical approach is also relevant as a predictive tool for the case where ion fractions only due to single H-C collisions could be effectively measured.

C. Band structure

Figure 6 shows the electronic band structure of the C_{60} ML deposited on Cu(111) (left) and the density of states (DOS) projected on the C_{60} ML (right), both calculated using the FIREBALL code. The projected DOS reveals the presence of states in the vicinity of the Fermi level, leading to a metallization of the film. This can be compared to the semiconductor character of thick C_{60} films, where the value of the highest occupied–lowest unoccupied molecular orbitals (HOMO-LUMO) gap is around 2 eV. The band states originated from the hybridization of the C_{60} molecular states and the Cu orbitals show a more pronounced dependence with $k_{//}$ (that is, dispersion) when contrasted to that of a thick C_{60} layer [6], but lower than that of pristine Cu(111) [42]. As Eq. (4) indicates, different incoming and exit projectile velocity components alter the influence of a particular region of the surface band structure on the charge exchange process. The slight but noticeable dispersion in $k_{//}$ of the C_{60} monolayer band structure (specially around the Γ point) suggests that minor differences are expected in the ion fractions resulting from H-C collisions for different geometrical incoming and exit angles (keeping the backscattering condition).

The well-defined LEED pattern obtained for the target surface (see Fig. 1) allows us to identify the scattering plane (or azimuthal orientation) used in the experiments. This plane corresponds to the $\overline{M}-\overline{\Gamma}-\overline{M}$ path in the first Brillouin zone of the 2D reciprocal lattice, as shown in the inset of Fig. 6. Other paths of the first Brillouin zone, such as $\overline{\Gamma}-\overline{K}$ or $\overline{K}-\overline{M}$ present similar dispersions in $k_{//}$. Therefore, only minor changes in the ion fractions originated in H-C collisions are foreseen if other azimuthal directions are explored.

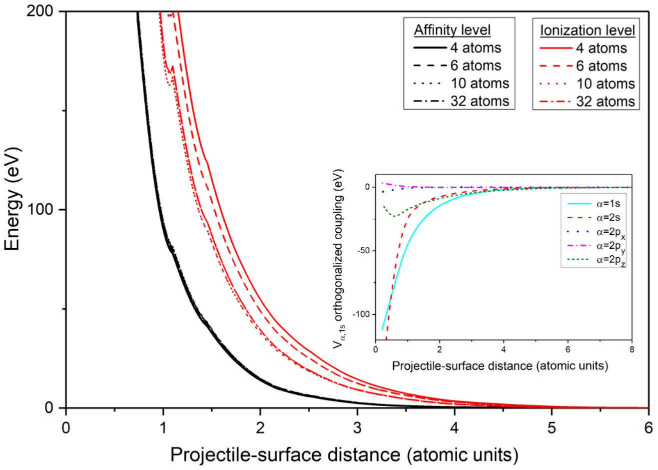

FIG. 7. Affinity and ionization projectile energy level widths as a function of the projectile-surface distance for different numbers of surface atoms considered. The orthogonalized $H_{1s} - C_\alpha$ coupling terms corresponding to the scatter atom (inset) are also shown.

1. Coupling terms, energy widths, and characteristic time analysis

The number of surface atoms relevant in the theoretical calculation, and therefore included in the summation of Eq. (4), depends on the projectile-target interaction extent and the collisional geometry. For example, grazing trajectories allow the projectile to interact with more surface atoms than in collisions with large incident and exit angles. Under our assumption of frontal collision for the theoretical calculations, the projectile is always on top of the scatter atom, and the relevant parameter is the vertical distance between the projectile ion and the scatter atom, z. As in our previous study involving a thick C_{60} film deposited on Cu(111) [6], we included here four C neighbors for the dynamical calculations: the scatter atom and its three nearest neighbors.

The ionization and affinity projectile level widths as a function of the ion-surface distance, calculated via Eq. (7), are plotted in Fig. 7 for different numbers of surface atoms considered. The inset of Fig. 7 shows the dependence of the coupling terms $V_{\alpha,1s}(\vec{R})$ between the $1s$ state of the projectile atom and the α states of the C scatter atom with the projectile-target distance. The coupling terms, $V_{\alpha,1s}(\vec{R})$, of the C surface atoms are orthogonalized by considering up to fourth nearest neighbors of the scatter atom (32 C atoms in total).

In Fig. 7 we show that the Anderson affinity width converges (within ~2%), including only four neighbors. However, a difference of ~10% between the converged value including 10 C atoms and that corresponding to four C atoms was found for the ionization level. This difference suggests that the inclusion of further neighbors in the calculation (up to ten C atoms, to achieve convergence within ~2%) would have been optimal for the study of the present system. Due to computational limitations, we included four C atoms in the dynamical calculation. We should also mention that the same number of neighbors (four) was found to be sufficient to accurately describe the scattering of protons with an HOPG surface [46,47,64], with similar C-C atom distances. In addition, although four C atoms directly interact with the projectile atom [Eq. (4)], the remaining C surface atoms indirectly enter

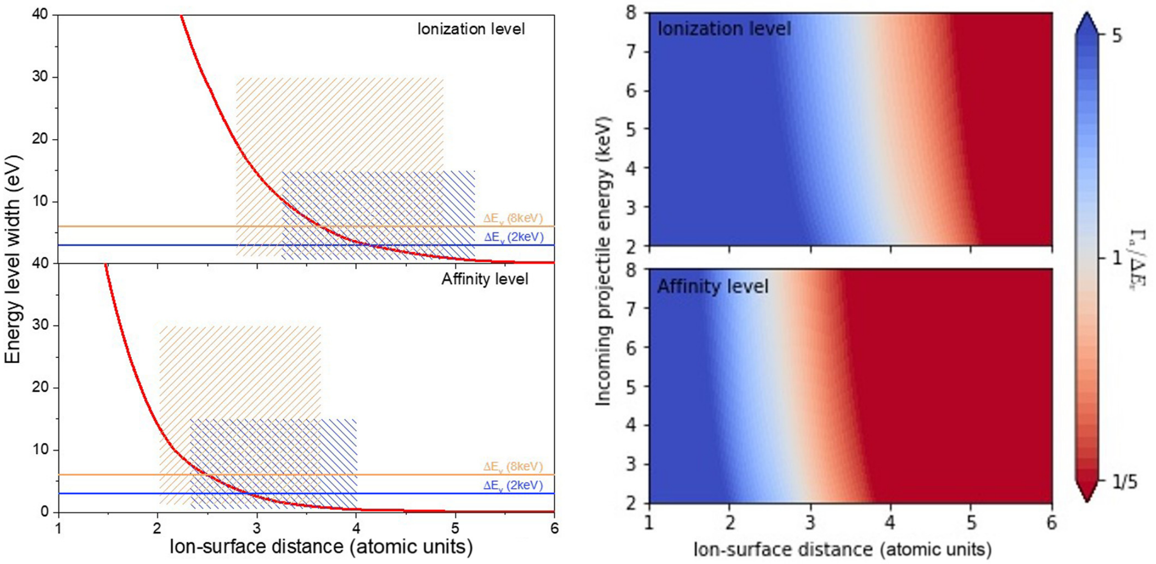

FIG. 8. Left: Interaction (Γ_a) and inherent velocity (ΔE_v) level widths comparison for ionization (upper panel) and affinity (lower panel) energy levels and for the maximum (8 keV) and minimum (2 keV) incoming projectile energies. The widths of the shaded boxes for a given energy allow us to estimate the spatial region where the corresponding level is active for charge exchange. The upper and lower limits of the shaded rectangles fulfill the criteria $\frac{\Gamma_a}{\Delta E_v} = 5^{-1}$ and $\frac{\Gamma_a}{\Delta E_v} = 5$, respectively. The values $\Delta E_v(2\,\text{keV}) = 3\,\text{eV}$ and $\Delta E_v(8\,\text{keV}) = 6\,\text{eV}$ are the level widths inherent to the velocity of the projectile [6]. Right: Color maps allowing us to visualize the spatial region where the ionization and affinity levels are operative for effective charge transfer (bright whitish regions). Outside these regions, the system is found in the low and high projectile velocity regimes.

into the calculation through the density matrix of the surface [Eq. (3)].

The information provided in the inset of Fig. 7, related to the H-C coupling terms, can be summarized in three main points: (i) a strong localization of the hopping terms, becoming remarkably large for projectile-surface distances lower than 2 a.u. (∼1 Å) and decaying to nearly zero for ion-surface distances larger than 4.5 a.u.; (ii) non-null $V_{2p_x,1s}$ and $V_{2p_y,1s}$ as a consequence of the orthogonalization over a nonflat arrange of 32 atoms in the C_{60} molecule; and (iii) the predominance of $V_{2p_z,1s}$ over $V_{2p_x,1s}$ and $V_{2p_y,1s}$. Remark (i) supports the choice of up to first nearest neighbors (four C atoms in total) with direct interaction with the projectile, since the second and upper nearest neighbors are at distances larger than 4.5 a.u. from the scatter atom; remark (ii) is related to the distinct topology of the C_{60} monolayer when compared to other previously studied carbon-based flat surfaces such as HOPG [46,47,59], and remark (iii) is a consequence of the normal collision situation assumed in our calculation.

The electronic projectile energy levels are broadened due to two factors: the interaction with the surface (Γ_a) and the level width inherent to the projectile motion, determined by the perpendicular component of the projectile velocity ($\Delta E_v \approx v_\perp/2$, in atomic units). As shown in our previous study [6], these two parameters determine the collision and interaction times, respectively, which is convenient for the estimation of the spatial region where the projectile-surface charge exchange is effective. Within this region, the interaction and inherent energy widths are comparable (we took $5^{-1} \leqslant \frac{\Delta E_v}{\Gamma_a} \leqslant 5$ as a criterion). Outside this region, instead, the regimes of large projectile velocity ($\frac{\Delta E_v}{\Gamma_a} > 5$) and low projectile velocity ($\frac{\Delta E_v}{\Gamma_a} < 5^{-1}$) are characterized by a very short time to allow the projectile-surface electronic exchange, and a loss of memory of the initial charge state leading to a highly varying projectile charge state, respectively. Figure 8 (left panel) shows a comparison of Γ_a and ΔE_v for the ionization and affinity energy levels, calculated for the inferior (2 keV) and superior (8 keV) limits of the explored energy. The shaded boxes are plotted to show the spatial region where each energy level is operative for electronic charge exchange. In the right panel of Fig. 8, contour plots show the $\frac{\Gamma_a}{\Delta E_v}$ ratio dependence with the projectile incoming energy and the ion-surface distance for the ionization and affinity levels. These plots help to visualize the regions where the low- (blue) and high- (red) velocity conditions are fulfilled, and the range of ion-surface distances (z) where each projectile electronic level is active for effective charge transfer (brighter regions).

The plots presented in Fig. 8 allows us to envisage some important details of the charge exchange during the projectile-surface collision. Given that the distances of closest approach range from 0.2 a.u. (for 8 keV) to 0.5 a.u. (for 2 keV) [6], in the spatial region closer to the surface ($0.2\,\text{a.u.} < z < 1.5\,\text{a.u.}$) the low-velocity regime condition is fulfilled for the whole projectile energy range. The loss of memory of the initial projectile charge state in this region close to the surface implies that the scattered ion fraction is predominantly defined in the exit trajectory. The opposite situation occurs at H-C distances larger than 5 a.u., where the final projectile charge state is already completely defined.

Considering both electronic levels, the spatial region where the resonant charge transfer takes place has a range of $2\,\text{a.u.} < z < 5.2\,\text{a.u.}$ for 2 keV, and $1.5\,\text{a.u.} < z < 4.5\,\text{a.u.}$ for 8 keV. As expected, this region is closer to the surface for higher projectile incoming energies. The size of the region where each level is operative for charge transfer is quite limited: about 2 a.u. irrespective of the projectile incoming energy. A reduced negative or positive ion formation is then expected after a highly probable initial neutralization of the H^+ projectile, due to the resonant position of the projectile ionization level with the surface valence band (see Fig. 6).

After the initial neutralization, the formation of negative ions requires the promotion of one electron of the valence band to the affinity projectile level. Thus, the affinity level width should be sufficiently large (>4 eV) to allow the access to the occupied states below the Fermi level. The spatial region where this situation is fulfilled is larger for higher incoming projectile energies: $2\ \text{a.u.} < z < 2.7\ \text{a.u}$ for 2 keV, and $1.5\ \text{a.u.} < z < 3.5\ \text{a.u.}$ for 8 keV (see lower panel of Fig. 8). However, the longer time spent within this region by slower projectiles could compensate the potential increase of negative ion formation with the projectile incoming energy.

Final positive projectile ions originate from (i) a certain survival probability of initial H^+ projectiles, expected to be very low and increasing with incoming projectile energy, and (ii) a reionization (electron loss) following the projectile neutralization in the incoming trajectory. Process (ii) requires a large ionization level width (>9 eV) for this level to reach the empty states of the conduction band. These level widths are available only in very limited spatial regions that grow with incoming energy: $3\ \text{a.u.} < z < 3.5\ \text{a.u.}$ for 2 keV, and $1.5\ \text{a.u.} < z < 3.5\ \text{a.u.}$ for 8 keV (see upper panel of Fig. 8). This process leads also to an increase of the positive ion fraction with the incoming projectile energy although, as it occurs in the negative ion formation, the shorter time spent by faster projectiles could counterbalance this trend. However, when compared to the negative ion formation, the extra process of the initial H^+ survival probability could explain the slight increase of the positive ions with the projectile incoming energy, not observed for the negative ion formation. Another important point that is derived from the previous analysis is that negative and positive ions are mostly formed in separated spatial regions which are similar in size. Negative ion formation mostly occurs in deeper (closer to the surface) regions when contrasted to that of positive ions.

2. *Theoretical results*

In Fig. 9 the theoretical results considering both experimental geometries explored are shown. Given the major incidence of projectile–copper substrate collisions in the experimental ion fractions, marked differences between theoretical and experimental results are expected.

For both geometries explored, the negative ion fractions show an oscillatinglike behavior mainly at low incoming energies and an almost constant character at higher energies. Unlike previous results for H^+ on a thick C_{60} film [6] and as anticipated in Sec. IV A 2, the negative ion fractions theoretically obtained for the H-C_{60} ML system are underestimated when compared to the experimental ones due to the major influence of H-Cu collisions in the measured ion fractions (H-Cu collisions produce higher negative ion fractions than H-C ones).

The calculated positive ion fractions also show some oscillations but they definitively increase with the projectile incoming energy mostly due to the reasons underlined in Sec. IV B 1. As expected, calculated positive ions are higher than measured positive ions due to, again, the large influence of H-Cu collisions in the measured ion fractions that leads to a lower production of positive ions when compared to H-C collisions (see Fig. 4).

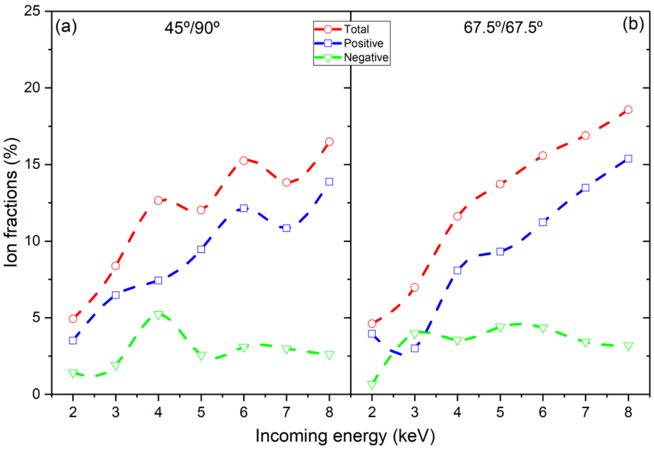

FIG. 9. Theoretical results for both experimental geometries explored: 45° and 90° (a) and 67.5° and 67.5° (b).

3. *Detailed comparison with previously studied systems*

The present contribution constitutes the last part of a trilogy of papers devoted to the understanding of the charge transfer processes in collisions of an H^+ projectile and three different surfaces: Cu(111) [42,55], a thick C_{60} film (approximately three layers) deposited on a Cu(111) substrate [6], and the present study of a C_{60} monolayer grown on the same substrate. The comparative analysis between these three systems provides valuable information on how the substrate influences the final charge state of the hydrogen projectile, and sheds some light on the relevance of the physical ingredients involved in the dynamic charge transfer process.

The left panel of Fig. 10 shows the theoretical final positive and negative ion fractions for the three systems studied in both experimental configurations. In the right panel of the same figure we can observe the analogous experimental results. Note that both ion fractions were referred to differently: “calculated ion fraction” and “measured ion fraction,” since the measured ion fraction presents extra contributions from multiple collisions, not considered in the theoretical ion fraction.

Considering the theoretical results for both geometrical configurations in the left panel of Fig. 10, a higher negative hydrogen ion production is observed after protons are scattered by a Cu(111) surface when compared to that of H-C collisions. On the other hand, a predominance of positive scattered ions, especially for higher energies, is theoretically obtained for both C_{60} films. When comparing both carbonaceous samples, only minor differences are obtained for both films grown when compared in trend and in magnitude for both geometric configurations.

Comparing left (theoretical) and right (experimental) panels of Fig. 10, we can observe that while the measured ion fractions in the scattering from the thick C_{60} film satisfactorily agree with our theoretical predictions [6], in the case of a

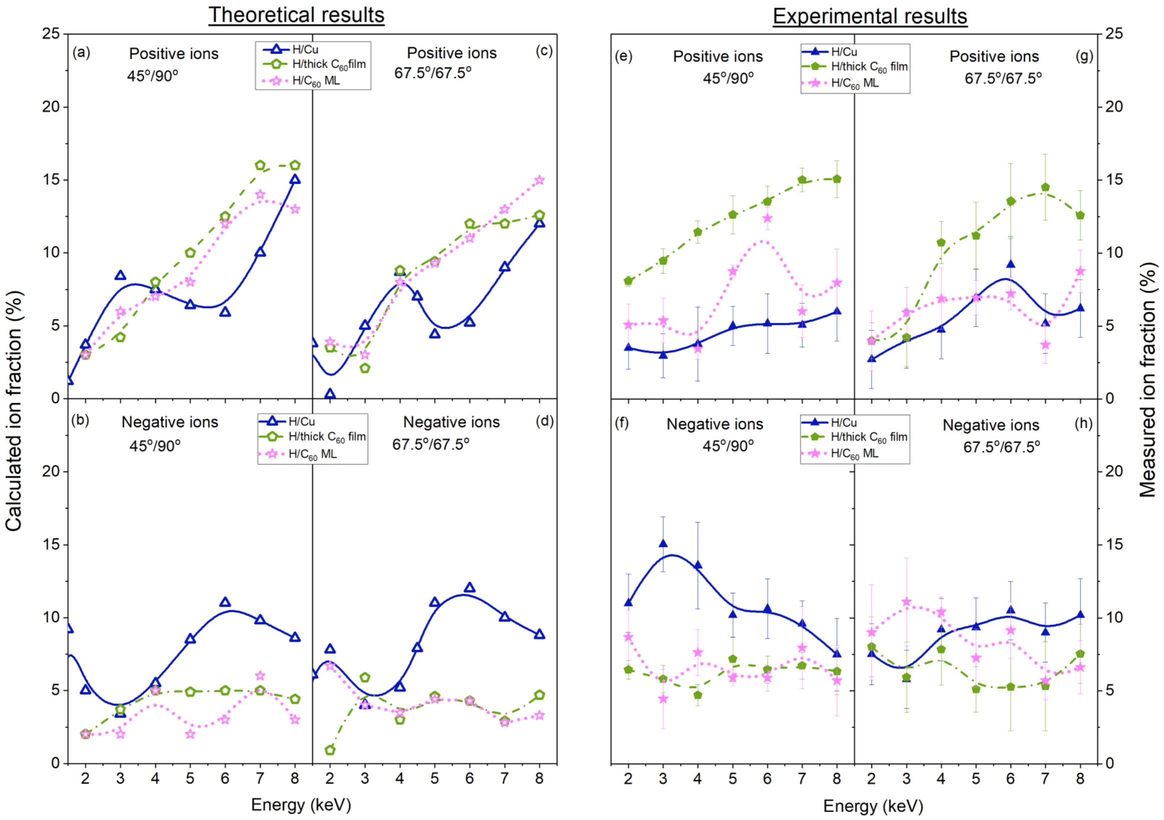

FIG. 10. Theoretical (left panel) and experimental (right panel) hydrogen positive and negative ion fractions scattered by Cu(111) [42], a thick C_{60} film deposited on Cu(111) [6], and a C_{60} monolayer grown on the same substrate. Results are shown for the two different incoming (exit) angles: 45° (90°) [theoretical (a), (b) and experimental (e), (f) correspond to positive and negative ion fractions, respectively] and 67.5° (67.5°) [theoretical (c), (d) and experimental (g), (h) correspond to the positive and negative ion fractions, respectively]. In both panels, the lines are intended to guide the eyes.

C_{60} ML the departure of the measured ion fractions from the calculated ones is evident. The similarities between measured ion fractions in the scattering by Cu(111) and by C_{60} ML, and the more pronounced dependence on the collision geometry, induce us to think that the multiple collisions with the substrate atoms have a major influence on the final charge state of the hydrogen projectiles scattered by the C_{60} ML deposited on Cu(111).

To understand the theoretical results, Fig. 11 shows a comparison between the band structures (left) and the total density of states (right) of the three studied systems.

The left panel of Fig. 11 shows clear differences in the dispersion in $k_{//}$ between the clean Cu(111) surface and the carbonaceous films. While the band states of the copper surface present a strong dependence with $k_{//}$, the other two films mostly show low-dispersive flat bands. As discussed in Ref. [42], the more dispersive character of the Cu(111) electronic band structure and especially the existence of a localized surface state (Fig. 11) can be directly associated to a major relevance of the projectile incoming trajectory in the final ion fraction. A final charge state more sensitive to the projectile trajectory would certainly lead to higher discrepancies between theoretical and experimental results, mainly due to the normal collision assumption made in the theoretical model, which is not satisfied in the experiment. When comparing both C_{60} films, the monolayer is slightly more dispersive than the thick C_{60} film. Even when the final projectile charge state is largely defined at the exit projectile trajectory for both systems, the more dispersive character of the C_{60} monolayer band structure suggests a poorer theoretical description of a potential experiment where only single H-C collisions are considered in the ion fraction determination.

In the right panel of Fig. 11, we can observe the total DOS (for C_{60} films, the states are summed over states and atoms of the whole C_{60} molecule) calculated for the three systems. When contrasting both carbonaceous films, the total DOS of the C_{60} ML shows, in general, a broadening and shifting of the peaks due to the hybridization with the substrate Cu(111) band states, when compared with the thick C_{60} film layer result. In addition, an interfacial state emerges in the surrounding of the surface Fermi level (at around −0.25 eV), associated to the partial filling of the pure C_{60} LUMO due to the adsorbate-substrate charge transfer and consistent with previous observations [65,66]. The separation between the most important peaks, such as HOMO and HOMO–1 or LUMO and LUMO+1 are underestimated in our calculated DOS when contrasted to experimental measurements [37]. Despite these differences, which could be a potential source of error for the applied model, the calculated density of states reproduces reasonably well the main features of the measured DOS [37].

The approximately similar calculated ion fractions obtained for both carbonaceous films allow us to arrive to a

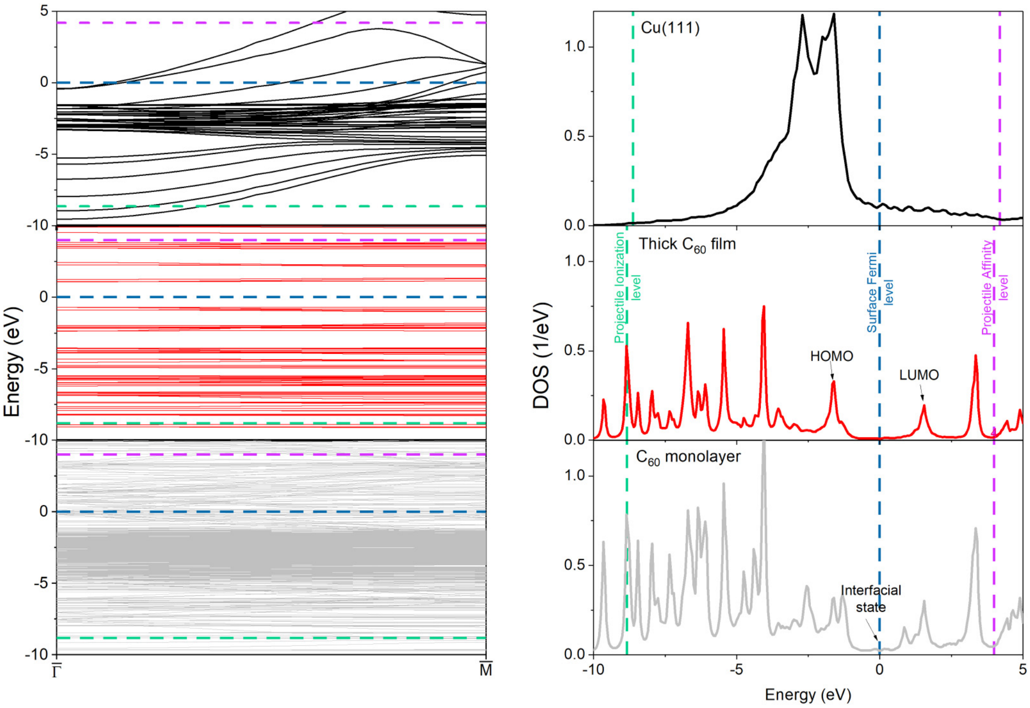

FIG. 11. Left: Calculated electronic band structure for the $\overline{\Gamma}-\overline{M}$ path of the Cu(111) surface (upper panel), a thick C$_{60}$ film deposited on a Cu(111) substrate (middle panel), and a C$_{60}$ monolayer deposited on the same substrate (lower panel). Right: The corresponding total density of states. For C$_{60}$ films, the states are summed over states and atoms of the whole C$_{60}$ molecule. The surface Fermi level and the projectile ionization and affinity levels are also indicated.

relevant conclusion: The distance between the copper substrate and the upper C atom of the C$_{60}$ molecule is still large enough to introduce minor changes in these C atom local DOS and, consequently, only slight modifications in the scattered final ion fraction. To explore if the local DOS of the other C atoms of the C$_{60}$ molecule are affected by the nearby copper substrate, in Fig. 12 we show the calculated local DOS (summed over states) for three different carbon atoms of the C$_{60}$ molecule, located at different distances of the Cu(111) substrate. As shown in the inset of the upper panel of Fig. 12, atom 1 belongs to the uppermost C$_{60}$ atomic plane, while atoms 2 and 3 are in the second and third top atomic planes of the C$_{60}$ molecule, respectively. Due to their location, these three atoms are possible direct scattering centers for the colliding hydrogen atom. The local DOS are comparatively shown for equivalent carbon atoms of the C$_{60}$ monolayer (upper panel) and the thick C$_{60}$ film (lower panel).

In the upper panel of Fig. 12 we can observe an expected result: relative to the uppermost C atom (atom 1), the local DOS of the carbon atoms are more altered by the substrate when the atoms are closer to it. The hybridization of the C states with the Cu(111) d band increases the density of states around the Fermi level and introduces modifications in the peaks distribution, especially within the energy region where the density of states of the substrate is larger. These variations in the local DOS are practically not observed for the thick C$_{60}$ film (lower panel), given that the distance of the three carbon atoms to the substrate is sufficiently large (about three stacked C$_{60}$ monolayers) to prevent the hybridization between C and Cu states. Outside the energy region where the Cu(111) DOS is important (below −6 eV or above 2 eV), the influence of the substrate is definitively minor, leading to local DOS rather similar for the three C atoms considered and almost the same for the monolayer and the thick C$_{60}$ films.

According to these results, in the C$_{60}$ monolayer, each scattering center may affect differently the final charge state of the scattered projectile. Then, the theoretical assumption of a unique scattering center is only valid for the thick C$_{60}$ film. In this way, an improved calculation should contain information about the charge exchange for all the possible scattering centers, weighted by the collision probability of the hydrogen projectile with the corresponding scattering center. Preliminary calculations (not shown) reveal that even when the ion fractions depend on the C atom taken as the scattering center, the average magnitude and trend are not strongly altered.

Then, from the full analysis of the theoretical results, we can conclude that if only binary H-C collisions are involved, the ion fractions for the two C$_{60}$ films are very similar, with minor differences attributable to the electronic band structure of each system.

V. CONCLUSIONS

Total, positive, and negative ion fractions of H$^+$ ions scattered by a C$_{60}$ monolayer deposited on a Cu(111) substrate were experimentally determined for different projectile incoming energies in the low-energy range (from 2 to 8 keV) for two incoming and exit angles in a backscattering configuration. Given the large range of hydrogen ions at the explored energies, the measured ion fractions include projectiles backscattered from substrate copper atoms that pass

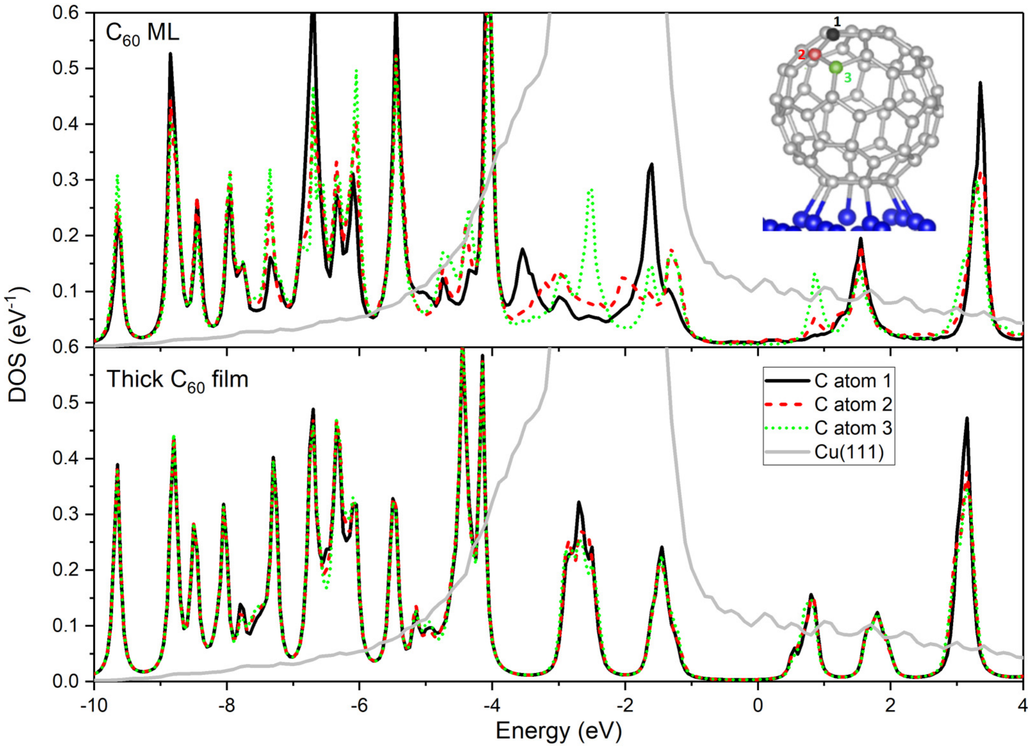

FIG. 12. Local DOS for the three atoms labeled as 1–3 in the C_{60} molecule (inset, upper panel) placed at different distances from the substrate. The total DOS of Cu(111) is plotted to indicate the energy region where the substrate is expected to have a higher influence on the DOS of the carbon atoms. Results are compared for the C_{60} monolayer (upper panel) and the thick C_{60} film (lower panel).

through the C_{60} ML film before being detected. The ion fractions obtained barely depend on the geometrical configuration. Positive and negative ion fractions are similar in the whole energy range, showing fluctuations that prevent us from outlining a well-defined trend. The negative ion fraction is nearly constant (about 7%) for the normal exit configuration and shows a slight decrease with the incoming energy for the specular configuration. Positive ion fractions, instead, slightly increase with the projectile incoming energy.

A direct comparison with other related studied systems, such as H-HOPG, H-Cu(111), and H-C_{60} thick film, allows us to conclude that, unlike the H-C_{60} thick film, the ion fractions measured are severely affected by the charge exchange produced between the direct collisions of H projectiles with the copper substrate atoms.

Theoretical calculations of the scattered ion fractions were performed using a quantum mechanical formalism based on the Anderson Hamiltonian, where a normal projectile-surface collision is assumed and correlation is included for the three possible projectile charge states. In contrast with the experimental situation, in our model we assume that only single binary H-C collisions are relevant for electronic exchange, preventing then, a direct comparison between theoretical and experimental results.

The assessment of characteristic times allows us to extract valuable information on how the charge exchange process takes place in this system. The final charge state is essentially defined at the exit trajectory of the projectile in a limited region where the ion-surface distance ranges from 1.5 to 3.5 a.u.. Negative ion formation occurs closer to C atoms of the surface in a different spatial region where positive ions are formed.

Theoretical results from the present system were directly compared with analogous results from the H-Cu and on H-thick C_{60} film. The direct comparison allows us to conclude that the distance between copper substrate atoms and the most exposed C atom of the C_{60} molecule is not short enough to cause any relevant change in the final calculated ion fraction. However, the analysis of the surface band structure and the surface projected local DOS on each C atom shows that, unlike the thick C_{60} film, the substrate alters the electronic structure of the C_{60} monolayer conferring metallic properties to it, and significantly changes the local DOS of closer carbon atoms that are potential scattering centers. The existence of nonequivalent scattering centers becomes then a relevant feature for the ion fraction calculation, proper to the C_{60} monolayer that is not present in the H-thick C_{60} film or H-Cu.

The calculations performed for the present system should be considered as a valuable initial approach and as a predictive tool for experiments intended to obtain the final scattered ion fraction due to single H-C collisions. In this system, the inclusion in the model of electronic exchange in multiple scattering of H projectiles by copper substrate atoms and carbon atoms of the C_{60} film is certainly necessary for an accurate description of the experimental findings.

ACKNOWLEDGMENTS

This work was supported by CONICET through PIP Grant No. 11220150100546CO; U.N.L. through CAI+D No.

50620190100034LI; and ANPCyT through PICT No. 2019-2019-03493. C.G. acknowledges financial support from the Community of Madrid through the project NANOMAG-COST CM-PS2018/NMT-4321 and the computer resources at Lusitania II and the technical support provided by the Centro Extremeño de investigación, Innovación Tecnológica y Supercomputación (CENITS), Projects FI-2020-2-0022 and FI-2020-3-0033.

---

[1] C. Salvo, P. Karmakar, and J. Yarmoff, Inhomogeneous charge distribution across gold nanoclusters measured by scattered low energy alkali ions, Phys. Rev. B **98**, 035437 (2018).

[2] D. Primetzhofer, M. Spitz, E. Taglauer, and P. Bauer, Resonant charge transfer in low-energy ion scattering: Information depth in the reionization regime, Surf. Sci. **605**, 1913 (2011).

[3] A. G. Borisov, A. K. Kazansky, and J. P. Gauyacq, Resonant charge transfer in ion-metal surface collisions: Effect of a projected band gap in the H$^-$-Cu(111) system, Phys. Rev. B **59**, 10935 (1999).

[4] J. P. Gauyacq and A. G. Borisov, Charge transfer in atom-surface collisions: Effect of the presence of adsorbates on the surface, J. Phys.: Condens. Matter **10**, 6585 (1998).

[5] A. G. Borisov, D. Teillet-Billy, J. P. Gauyacq, H. Winter, and G. Dierkes, Resonant charge transfer in grazing scattering of alkali-metal ions from an Al(111) surface, Phys. Rev. B **54**, 17166 (1996).

[6] M. Tacca, V. Quintero Riascos, R. Vidal, C. Gonzalez, F. Bonetto, and E. C. Goldberg, Charge transfer in low-energy collisions of protons with a thick C$_{60}$ film, J. Phys. Chem. C **124**, 3632 (2020).

[7] P. Liu *et al.*, Anomalous neutralization characteristics in Na+ neutralization on Al(111) surfaces, Phys. Rev. A **101**, 032706 (2020).

[8] Y. Yao, P. Shushkov, T. F. Miller, and K. P. Giapis, Direct dioxygen evolution in collisions of carbon dioxide with surfaces, Nat. Commun. **10**, 2294 (2019).

[9] M. A. Romero, A. Iglesias-García, E. A. García, and E. C. Goldberg, Hydrogen ion scattering from a potassium impurity adsorbed on graphene, Phys. Rev. B **100**, 085432 (2019).

[10] A. Mitrushchenkov, M. Guitou, A. K. Belyaev, Y. V. Voronov, and N. Feautrier, Inelastic excitation and charge transfer processes for oxygen in collision with H atoms, J. Chem. Phys. **150**, 064312 (2019).

[11] A. D. Dörfler, P. Eberle, D. Koner, M. Tomza, M. Meuwly, and S. Willitsch, Long-range versus short-range effects in cold molecular ion-neutral collisions, Nat. Commun. **10**, 5429 (2019).

[12] A. M. Amarsi and P. S. Barklem, Excitation and charge transfer in low-energy hydrogen atom collisions with neutral carbon and nitrogen, Astron. Astrophys. **625**, A78 (2019).

[13] L. Gao *et al.*, Dynamical resonant neutralization of low-energy N+ ions scattered from Au(111), Pd(111), Cu(111), and Cu(110) surfaces, Phys. Rev. A **96**, 052705 (2017).

[14] R. A. Wilhelm and P. L. Grande, Unraveling energy loss processes of low energy heavy ions in 2D materials, Commun. Phys. **2**, 89 (2019).

[15] S. Lohmann and D. Primetzhofer, Disparate Energy Scaling of Trajectory-Dependent Electronic Excitations for Slow Protons and He Ions, Phys. Rev. Lett. **124**, 096601 (2020).

[16] J. Lienemann, D. Blauth, S. Wethekam, M. Busch, H. Winter, P. Wurz, S. A. Fuselier, and E. Hertzberg, Negative ion formation during scattering of fast ions from diamond-like carbon surfaces, Nucl. Instrum. Methods Phys. Res., Sect. B **269**, 915 (2011).

[17] P. R. Chalker, Photochemical atomic layer deposition and etching, Surf. Coat. Technol. **291**, 258 (2016).

[18] V. Dudnikov and A. Dudnikov, Positronium negative ions for monitoring work functions of surface plasma source, in *Fifth International Symposium on Negative Ions, Beams and Sources (NIBS 2016)*, AIP Conf. Proc. No. 1869 (AIP, Melville, NY, 2017), p. 020007.

[19] J. R. Hiskes, A. Karo, and M. Gardner, Mechanism for negative-ion production in the surface-plasma negative-hydrogen-ion source, J. Appl. Phys. **47**, 3888 (1976).

[20] G.-J. Kroes, M. Pavanello, M. Blanco-Rey, M. Alducin, and D. J. Auerbach, *Ab initio* molecular dynamics calculations on scattering of hyperthermal H atoms from Cu(111) and Au(111), J. Chem. Phys. **141**, 054705 (2014).

[21] H. R. J. ter Veen, T. Kim, I. E. Wachs, and H. H. Brongersma, Applications of high sensitivity-low energy ion scattering (HS-LEIS) in heterogeneous catalysis, Catal. Today **140**, 197 (2009).

[22] M. S. Dresselhaus, G. Dresselhaus, and P. C. Eklund, *Science of Fullerenes and Carbon Nanotubes* (Academic Press, San Diego, 1996).

[23] G. Lalwani and B. Sitharaman, Multifunctional fullerene and metallofullerene-based nanobiomaterials, Nano LIFE **03**, 1342003 (2013).

[24] S. Prylutska, C$_{60}$ fullerene enhances cisplatin anticancer activity and overcomes tumor cell drug resistance, Nano Res. **10**, 652 (2017).

[25] M. Jarvid, A. Johansson, R. Kroon, J. M. Bjuggren, H. Wutzel, V. Englund, S. Gubanski, M. R. Andersson, and C. Müller, A new application area for fullerenes: Voltage stabilizers for power cable insulation, Adv. Mater. **27**, 897 (2015).

[26] S. Z. Mousavi, S. Nafisi, and H. I. Maibach, Fullerene nanoparticle in dermatological and cosmetic applications, Nanomed. Nanotechnol. Biol. Med. **13**, 1071 (2017).

[27] H. K. H. Lee *et al.*, The role of fullerenes in the environmental stability of polymer:Fullerene solar cells, Energy Environ. Sci. **11**, 417 (2018).

[28] M. A. Cordiner *et al.*, Confirming interstellar $C_{60}{}^+$ using the hubble space telescope, Astroph. J. Lett. (ApJL) **875**, L28 (2019).

[29] M. Plihal, D. C. Langreth, and P. Nordlander, Effect of parallel velocity on the formation of a Kondo resonance in the atom-surface interaction, Phys. Rev. B **59**, 13322 (1999).

[30] J. Los and J. J. C. Geerlings, Charge exchange in atom-surface collisions, Phys. Rep. **190**, 133 (1990).

[31] J. N. M. Van Wunnik, R. Brako, K. Makoshi, and D. M. Newns, Effect of parallel velocity on charge fraction in ion-surface scattering, Surf. Sci. **126**, 618 (1983).

[32] O. Grizzi, E. A. Sánchez, J. E. Gayone, L. Guillemot, V. A. Esaulov, and R. A. Baragiola, Formation of autoionizing Ne**

in grazing collisions with an Al(111) surface, Surf. Sci. **469**, 71 (2000).

[33] L. Guillemot, S. Lacombe, M. Huels, T. Vu Ngoc, and V. A. Esaulov, Inelastic processes in Ne^+ collisions with a Mg surface; charge fractions and surface roughness, Nucl. Instrum. Methods Phys. Res., Sect. B **90**, 270 (1994).

[34] W.-j. Li, P. Wang, X.-X. Wang, J.-O. Wang, R. Wu, H.-J. Qian, K. Ibrahim, H.-Y. Li, and H.-N. Li, Fullerene film on metal surface: Diffusion of metal atoms and interface model, Appl. Phys. Lett. **104**, 191606 (2014).

[35] M. B. Casu, Growth, structure, and electronic properties in organic thin films deposited on metal surfaces investigated by low energy electron microscopy and photoelectron emission microscopy, J. Electron Spectrosc. Relat. Phenom. **204**, 39 (2015).

[36] A. Groß, in *Theoretical Surface Science: A Microscopic Perspective*, edited by A. Groß (Springer, Berlin, 2009), p. 59.

[37] A. J. Gibson, R. H. Temperton, K. Handrup, and J. N. O'Shea, Resonant core spectroscopies of the charge transfer interactions between C_{60} and the surfaces of Au(111), Ag(111), Cu(111) and Pt(111), Surf. Sci. **657**, 69 (2017).

[38] A. C. Rosenfeldt, B. Göhler, and H. Zacharias, Time-resolved photoelectron spectroscopy of low-energy excitations of 4 × 4 C_{60}/Cu(111), J. Chem. Phys. **133**, 234704 (2010).

[39] G. Dutton and X. Y. Zhu, Unoccupied states in C_{60} thin films probed by two-photon photoemission, J. Phys. Chem. B **106**, 5975 (2002).

[40] D. Primetzhofer, S. N. Markin, J. I. Juaristi, E. Taglauer, and P. Bauer, Crystal Effects in the Neutralization of He^+ Ions in the Low Energy Ion Scattering Regime, Phys. Rev. Lett. **100**, 213201 (2008).

[41] D. Primetzhofer, M. Spitz, S. N. Markin, E. Taglauer, and P. Bauer, Influence of surface structure and composition on neutralization of He^+ ions scattered from noble metals and alloy surfaces, Phys. Rev. B **80**, 125425 (2009).

[42] V. Q. Riascos, M. Tacca, R. Vidal, C. Gonzalez, E. C. Goldberg, and F. Bonetto, Band structure effects on the charge exchange processes in H^+ colliding with a Cu(111) surface, J. Phys. Chem. C **122**, 28192 (2018).

[43] F. Bonetto, R. A. Vidal, V. Q. Riascos, C. J. Bonin, and J. Ferrón, Growth, thermal desorption and low dose ion bombardment damage of C_{60} films deposited on Cu(111), J. Phys. Commun. **1**, 045004 (2017).

[44] P. G. Bolcatto, E. C. Goldberg, and M. C. G. Passeggi, Interaction between atoms and surfaces: A bond-pair description based on an extended Anderson model, Phys. Rev. B **58**, 5007 (1998).

[45] M. A. Romero, F. Flores, and E. C. Goldberg, Effective treatment of charge and spin fluctuations in dynamical and static atom-surface interactions, Phys. Rev. B **80**, 235427 (2009).

[46] F. J. Bonetto, M. A. Romero, A. Iglesias-García, R. A. Vidal, and E. C. Goldberg, Time-energy uncertainty and electronic correlation in H^+-graphite collisions, J. Phys. Chem. C **119**, 3124 (2015).

[47] R. A. Vidal, F. Bonetto, J. Ferrón, M. A. Romero, E. A. García, and E. C. Goldberg, Electron capture and loss in the scattering of H^+ from HOPG graphite, Surf. Sci. **605**, 18 (2011).

[48] G. Xu, X.-Q. Shi, R. Q. Zhang, W. W. Pai, H. T. Jeng, and M. A. Van Hove, Detailed low-energy electron diffraction analysis of the (4 × 4) surface structure of C_{60} on Cu(111): Seven-atom-vacancy reconstruction, Phys. Rev. B **86**, 075419 (2012).

[49] S. P. Tear, K. Roll, and M. Prutton, A comparison of reliability (R) factors in a LEED structural analysis of the copper (111) surface, J. Phys. C: Solid State Phys. **14**, 3297 (1981).

[50] F. Jona, LEED crystallography, J. Phys. C: Solid State Phys. **11**, 4271 (1978).

[51] P. Bauer, in *Surface and Thin Film Analysis: A Compendium of Principles, Instrumentation, and Applications.*, edited by G. Friedbacher and H. Bubert (John Wiley & Sons, New York, 2011).

[52] H. H. Brongersma, M. Draxler, M. de Ridder, and P. Bauer, Surface composition analysis by low-energy ion scattering, Surf. Sci. Rep. **62**, 63 (2007).

[53] O. Grizzi, M. Shi, H. Bu, and J. W. Rabalais, Time-of-flight scattering and recoiling spectrometer (TOF-SARS) for surface analysis, Rev. Sci. Instrum. **61**, 740 (1990).

[54] M. Maazouz, L. Guillemot, T. Schlatholter, S. Ustaze, and V. A. Esaulov, Electron capture and loss in the scattering of oxygen atoms and ions on Mg, Al, and Ag surfaces, Nucl. Instrum. Methods Phys. Res., Sect. B **125**, 283 (1997).

[55] R. Vidal, J. Ferrón, C. I. Meyer, V. Q. Riascos, and F. Bonetto, The influence of surface defects on the low energy scattering of Ar ions from a Cu(111) surface, Surf. Sci. **690**, 121482 (2019).

[56] J. F. Ziegler, M. D. Ziegler, and J. P. Biersack, SRIM—The stopping and range of ions in matter (2010), Nucl. Instrum. Methods Phys. Res. B **268**, 1818 (2010).

[57] D. Primetzhofer (private communication).

[58] F. Bonetto, M. A. Romero, E. A. García, R. A. Vidal, J. Ferrón, and E. C. Goldberg, Large neutral fractions in collisions of Li^+ with a highly oriented pyrolytic graphite surface: Resonant and auger mechanisms, Phys. Rev. B **78**, 075422 (2008).

[59] F. Bonetto, M. A. Romero, E. A. García, R. Vidal, J. Ferrón, and E. C. Goldberg, Relevant effects of localized atomic interactions and surface density of states on charge transfer in ion-surface collisions, Europhys. Lett. **80**, 53002 (2007).

[60] L.-L. Wang and H.-P. Cheng, Rotation, translation, charge transfer, and electronic structure of C_{60} on Cu(111) surface, Phys. Rev. B **69**, 045404 (2004).

[61] W. W. Pai, C.-L. Hsu, M. C. Lin, K. C. Lin, and T. B. Tang, Structural relaxation of adlayers in the presence of adsorbate-induced reconstruction: C_{60}-Cu(111), Phys. Rev. B **69**, 125405 (2004).

[62] J. P. Lewis *et al.*, Advances and applications in the FIREBALL *ab initio* tight-binding molecular-dynamics formalism, Phys. Status Solidi B **248**, 1989 (2011).

[63] L. V. Keldysh, Diagram technique for nonequilibrium processes, J. Exp. Theor. Phys. **20**, 1018 (1965).

[64] M. Romero, A. Iglesias-García, and E. C. Goldberg, Quantum-mechanical interference in charge exchange between hydrogen and graphene-like surfaces, J. Phys.: Condens. Matter **24**, 045004 (2012).

[65] A. Stróżecka, J. Mysliveček, and B. Voigtländer, Scanning tunneling microscopy and manipulation of C_{60} on Cu(111), Appl. Phys. A **87**, 475 (2007).

[66] K. D. Tsuei and P. D. Johnson, Charge transfer and a new image state of C_{60} on Cu(1 1 1) surface studied by inverse photoemission, Solid State Commun. **101**, 337 (1997).